communications earth & environment

Article

https://doi.org/10.1038/s43247-024-01577-3

Disruptions in thermohaline staircases caused by subsurface mesoscale eddies in the eastern Caribbean Sea

Check for updates

Shun Yang[1,2,4], Kun Zhang[1,2,4], Haibin Song[1,2] ✉, Barry Ruddick[3], Mengli Liu[1,2] & Linghan Meng[1,2]

Thermohaline staircases and mesoscale eddies play crucial roles in the transport of heat, salt, and nutrients in the ocean, yet their complex relationship remains unclear due to the limitations in observational resolution and lateral range. Here, utilizing high spatial resolution seismic images with a total length of 2518 km, we show the widespread occurrence of thermohaline staircases in the eastern Caribbean Sea and demonstrate their three-dimensional distribution. These staircases occupy about 70% of the total length of the seismic lines, with the remaining 30% occupied by six subsurface mesoscale eddies. These staircases are disrupted and interrupted due to the enhanced turbulent diffusivity driven by the vertical shear of these eddies. The numerous high-resolution seismic observations presented herein enhance our comprehension of the interplay between staircases and multiscale oceanic dynamical processes.

Thermohaline staircases are stepped structures consisting of alternating thick mixed layers and thin high-gradient interfaces[1–4]. They are associated with double-diffusive processes. Thermohaline staircases in the diffusive-convective regime commonly occur at high latitudes, such as the Arctic Ocean[5–8], where fresh and cold waters overlie warmer and saltier waters. Double diffusion in the salt-finger regime is predominantly at lower latitudes, such as the tropical North Atlantic Ocean[4,9–11], the Caribbean Sea[12,13], and the Mediterranean Sea[14,15], where warm and salty waters overlie fresher and colder waters. Thermohaline staircases are often associated with enhanced diapycnal mixing in the thermocline[4], which can affect the transport of heat, salt, and nutrients in the ocean.

Thermohaline staircases typically exist in stable or weakly turbulent environments, such as central basins[5,15]. In the Eastern Caribbean Sea, many studies have confirmed the existence of thermohaline staircases[4,12,13,16,17]. The staircases in this region are believed to form through the double diffusion between the warm and salty subtropical subsurface water (SUW) and the underlying colder and fresher Antarctic Intermediate Water (AAIW)[4,16]. Most of the Caribbean staircases can maintain coherent structures for weeks to months[17]. In addition to the thermohaline staircases, widespread mesoscale eddies are also discovered in the Eastern Caribbean Sea[17–20]. After formation, these eddies are transported westward by background currents[19,21]. These eddies transport heat, CO_2, and nutrients in the ocean during advection.

Due to the limited number of observational samples and insufficient lateral resolution, there is still no consensus on the relationship between eddies and thermohaline staircases. One perspective suggests that thermohaline staircases form at the periphery of eddies[13,22]: the lateral gradient causes the interaction between the eddy core water and the background water around the eddy, forming interleaving structures, and ultimately evolving into thermohaline staircases. However, their data lacked adequate lateral resolution. Another viewpoint argues that the shear-induced by eddies disrupts thermohaline staircases[23,24], but small sample sizes and insufficient lateral observational ranges constrained these studies.

Thermohaline staircases are laterally coherent oceanographic phenomena. Owing to the constraints of horizontal sampling ranging from several to tens of kilometers, previous observations have generally struggled to intricately illustrate the lateral distribution of staircases. In recent years, there have been observations of Arctic staircases using high-frequency backscatter data, which, to a certain extent, enable the observation of spatial variations of shallow staircases[7,25]. However, due to the rapid energy decay of high-frequency acoustic observations, imaging of deeper water columns remains challenging, and these studies have yet to unveil the relationship between staircases and eddies.

Over the past two decades, an oceanographic observation technique called seismic oceanography (SO) has been increasingly applied in the studies of various ocean phenomena[26–29]. Based on the vertical contrasts in temperature and salinity within water columns (i.e., vertical temperature and salinity gradients), SO can achieve high-resolution imaging of vertical two-dimensional transects spanning tens of kilometers within the ocean interior in a matter of hours, covering the entire ocean depth[30,31]. With

[1]School of Ocean and Earth Science, Tongji University, Shanghai, China. [2]State Key Laboratory of Marine Geology, Tongji University, Shanghai, China. [3]Department of Oceanography, Dalhousie University, Halifax, NS, Canada. [4]These authors contributed equally: Shun Yang, Kun Zhang.
✉e-mail: hbsong@tongji.edu.cn

vertical and horizontal sampling intervals of about O (10) m, SO effectively addresses the limitations in horizontal sampling inherent in conventional oceanographic observations. SO has successfully observed numerous oceanic phenomena, including eddies[32–34] and thermohaline staircases[15,24,35,36]. Due to the high vertical gradients at the interfaces of staircases, these features are readily identified through the SO method.

In this work, we analyze thermohaline staircases and their association with eddies through the examination of 26 multi-channel seismic transects, covering a total length of 2518 km, collected in the Eastern Caribbean Sea from February to March 1995 (Fig. 1). These findings demonstrate the widespread prevalence (~70%) of staircases in this region, with several subsurface mesoscale eddies disrupting to these staircases. This disruption is attributed to turbulent mixing caused by vertical shear at the peripheries of these eddies. The numerous high-resolution observations presented herein enhance our comprehension of the interplay between staircases and multiscale oceanic dynamical processes.

Results

Identification of thermohaline staircases

As mentioned earlier, the formation of thermohaline staircases in the Caribbean Sea is attributed to the double diffusion between SUW and AAIW[4,16]. Within the depth range of about 150–700 m in the Eastern Caribbean Sea, the background Turner angle Tu maintains an average value between 45° and 90°, facilitating the formation of salt-finger staircases (Fig. 2d). Notably, this depth range precisely corresponds to the core depths of SUW and AAIW at 150 m and 700 m, respectively. Beyond this depth range, the remaining depths exhibit a predominantly stable state (excluding the sea surface). At a conductivity–temperature–depth (CTD) station (CTD No. 4, collected two years after seismic acquisition during the R/V Maurice Ewing EW9501 expedition; see Fig. 1), a typical salt-finger staircase was identified. This staircase extends roughly from about 350 m to 600 m (see Fig. 2), aligning closely with previous studies[13,16]. The temperature and salinity data from this CTD station reveal 10 interfaces of staircases, separated by 9 homogeneous mixed layers, extending from about 382 m to 551 m, with a cumulative thickness of about 169 m (Fig. 2). These interfaces are notably much thinner compared to the mixed layers. Each pair of mixed layers and interfaces constitutes a step, resulting in an average thickness of steps of 18.7 ± 2.6 m within this staircase. Note that the step thickness here is the thickness of a pair of a mixed layer and an interface not the thickness of the mixed layer. This is done to compare with the results of seismic data, as seismic data cannot distinguish narrow interfaces.

Employing the temperature and salinity from CTD No. 4, we generated a synthetic seismogram (see 'Methods'), as shown in Fig. 2h. Seismic reflections arise from the vertical gradients of temperature and salinity. Theoretically, interfaces with high gradients within thermohaline staircases, leading to the reflection coefficient on an order of 10^{-4}, can induce effective seismic reflections. The seismic data here have a vertical resolution of about 11 m (see 'Methods'), lower than the average thickness of steps (18.7 m) identified by CTD. Hence, steps can be discernible in the seismic data (Fig. 2). The reflection coefficients at the interfaces manifest as large negative values, while those at the mixed layers are near zero (Fig. 2g). The intense reflections within the depths of about 380 to 560 m in the synthetic seismogram represent the staircase (Fig. 2h). Negative values correspond to interfaces of the staircase, while positive values denote mixed layers (see 'Methods').

In seismic transects, thermohaline staircases exhibit high-amplitude reflections compared to background water due to their high-gradient interfaces[24,35]. Given their characteristic thin step thickness, typically less than 20 m in this region, these steps manifest as reflections with narrow vertical spacing[24,35]. Thermohaline staircases are often present as quasi-horizontal coherent structures[24,35]. Additionally, according to previous studies[13,16], these steps in the Eastern Caribbean Sea are primarily distributed at depths around 400–600 m. Based on these criteria, we identify the thermohaline staircases in actual seismic data in the following text.

Coherent thermohaline staircases

Figure 3 provides a striking three-dimensional view of the 26 seismic transects from the expedition EW9501. Thermohaline staircases are widely spread and lateral coherent (Fig. 3a), which are captured by many seismic lines in 3D space. They exhibit strong amplitude and thin-bedded

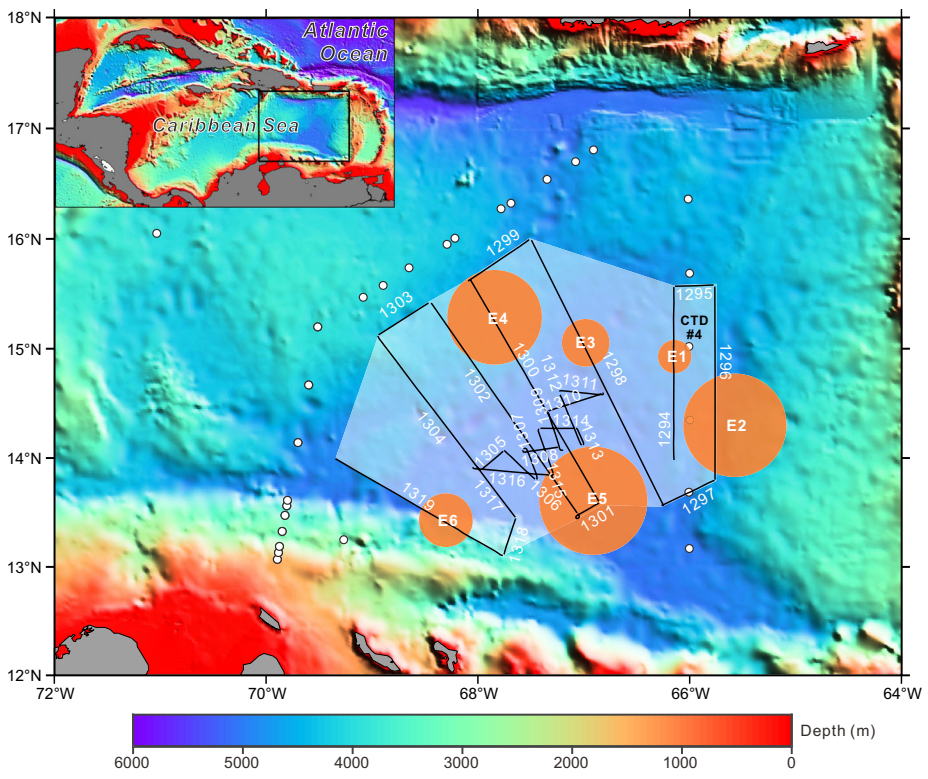

Fig. 1 | Map of seismic lines of expedition EW9501. The black lines are the trajectories of 26 seismic lines (marked 1294–1319, acquired from February 25 to March 9, 1995) from the expedition EW9501. Orange circles are the inferred locations of eddy cores (marked E1–E6). White circular markers are the positions of 39 historical conductivity–temperature–depth (CTD) casts in which CTD No. 4 was acquired on Aug 18, 1997. Gray polygons are the inferred region of staircase distribution. An inset in the upper-left corner provides the location of the study region.

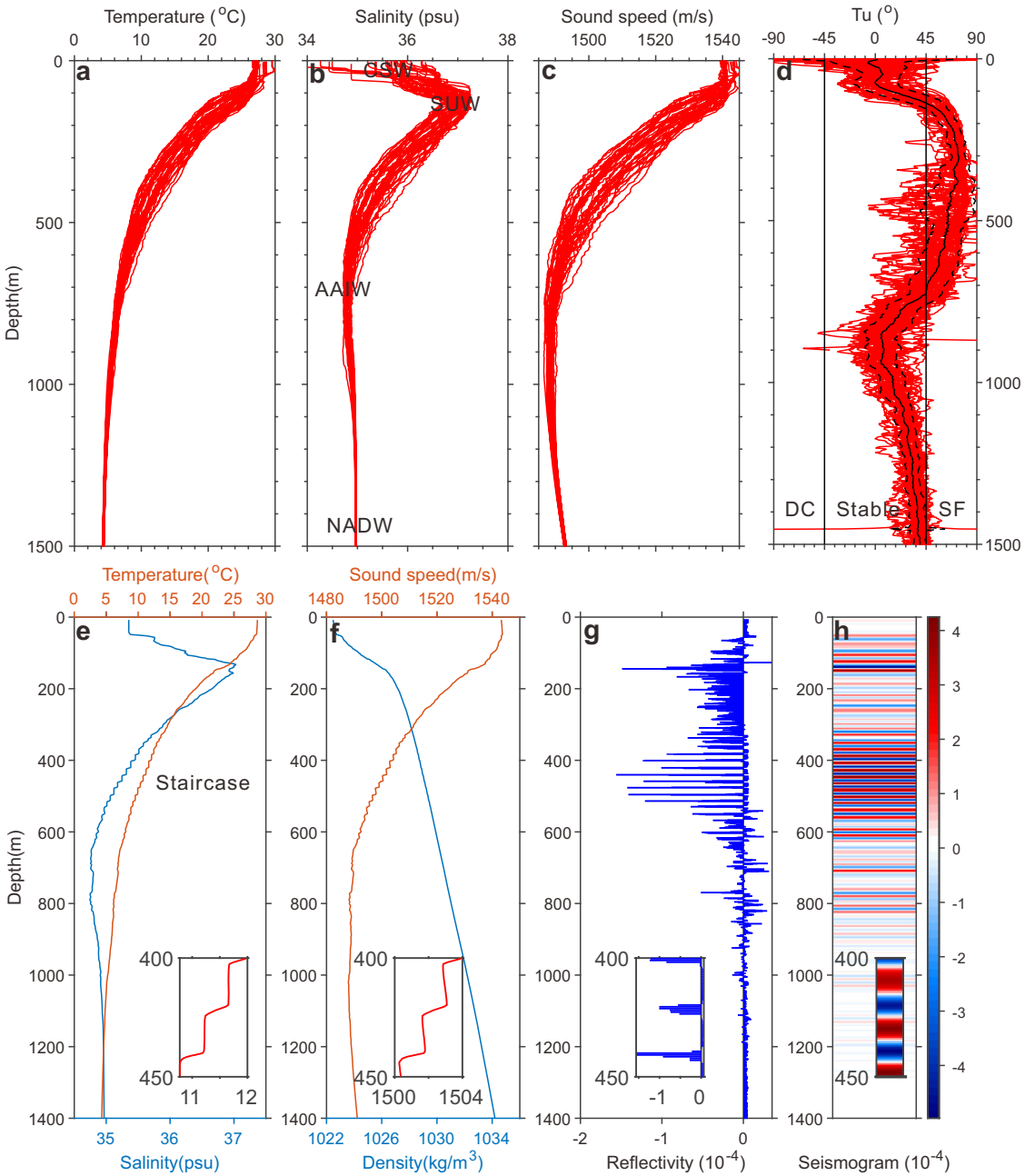

Fig. 2 | Hydrography in the Eastern Caribbean Sea and a synthetic seismogram. **a** Temperature, **b** salinity, and **c** sound speed derived from 39 historical CTD casts, as well as the calculated **d** Turner angle Tu. CSW is the Caribbean Surface Water; SUW is the Subtropical Underwater; AAIW is the Antarctic Intermediate Water; NADW is the North Atlantic Deep Water. The location of these abbreviations represents the central depths of the respective water masses. Tu variations in the water column define the following classification of the stability of the layers: $-90° < Tu < -45°$ for the diffusive convection regime (DC), $45° < Tu < 90°$ for the salt-finger regime (SF), $|Tu| < 45°$ for a stable state. The Turner angles of each CTD station are linearly smoothed over a 40 m depth bin. Black solid and dashed lines represent the mean values and standard deviations of these smoothed Turner angles, respectively. **e** Temperature (red) and salinity profile (blue), **f** sound speed (red) and density (blue) of CTD No. 4 (see Fig. 1 for the location), and **g** the reflection coefficients calculated from the sound speed and density of CTD No. 4. **h** Synthetic seismogram. Interfaces of the staircase are indicated by negative values (in blue), while mixed layers are represented by positive values (in red), as explained in section 'Methods'. The insets in **e**–**h** are the enlarged displays within the depths of 400–450 m.

reflections. As shown in Fig. 4, a series of seismic images reveal relatively intact and coherent staircases within depths of about 400–600 m. The lateral coherence of these staircases extends beyond 100 km (e.g., seismic transect 1304). Due to the removal of direct waves, the upper 150 m lacks effective reflectors. In these images, reflectors shallower than 400 m appear weaker; within the range from ~400 to 600 m, there are densely distributed, quasi-horizontal reflectors with high amplitudes, epitomizing the presence of staircases. The depth range of these staircases aligns with previous studies[13,16,18]. Between depths of 600–1000 m, reflectors diminish and exhibit more complex slopes. Reflectors deeper than 1000 m become increasingly faint, approaching a nearly blank state, attributed to the gradual decrease of stratification.

By tracking these reflectors, the subsequent calculation of step thickness is achievable, as illustrated in Supplementary Fig. 1. Across various seismic transects, the count of steps may be different, ranging from 8 to 10 layers (Supplementary Fig. 2). The computed thickness of these

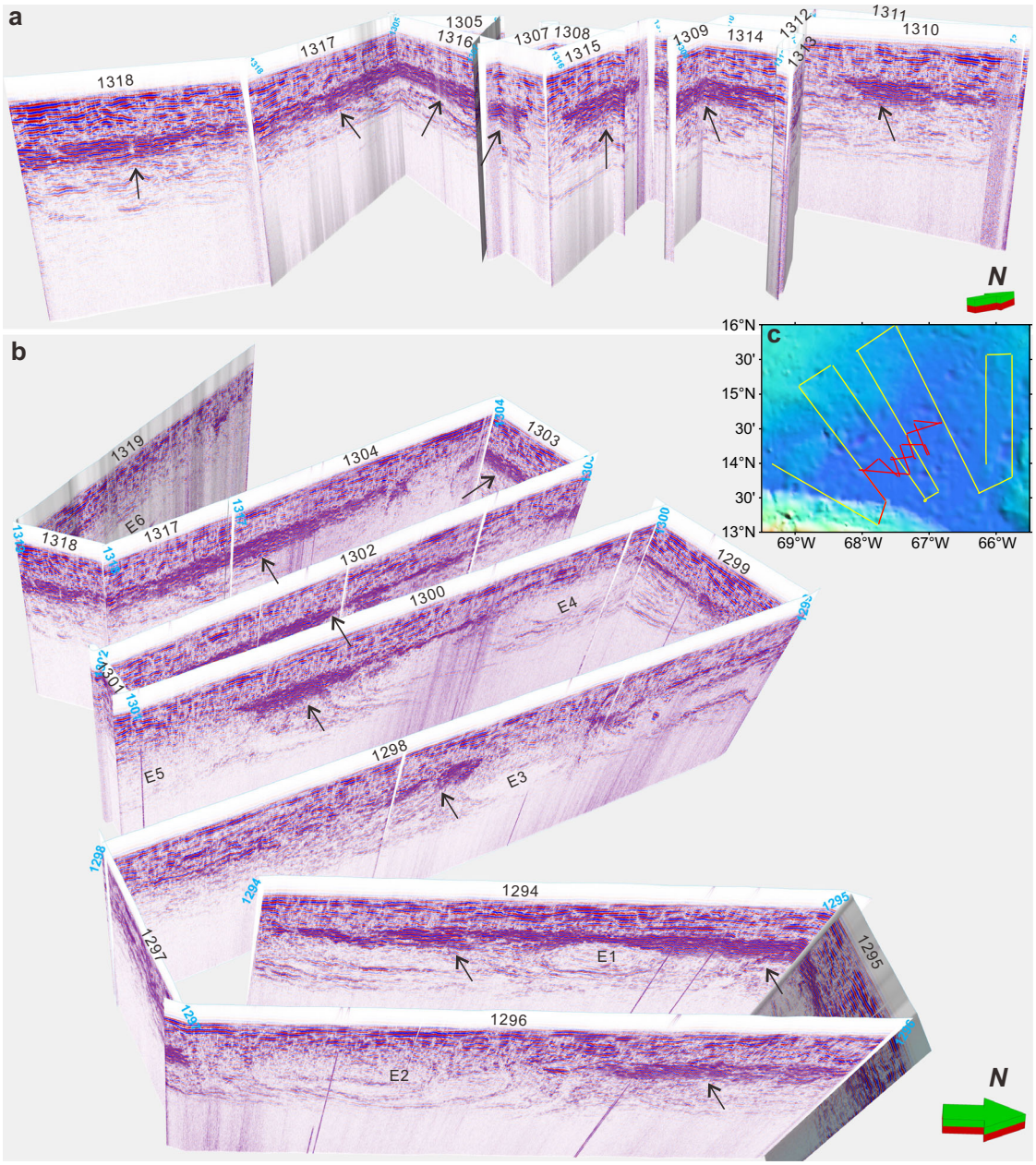

Fig. 3 | Three-dimensional view of seismic images from the expedition EW9501. **a** Short seismic images illustrate coherent thermohaline staircases. Images have a vertical exaggeration of 25. **b** Long seismic images reveal the distribution of eddies and their disruption on thermohaline staircases. Images have a vertical exaggeration of 50. Seismic line numbers are labeled (blue numbers indicate the starting position of seismic lines). Arrows point to the positions of the main staircases. E1–6 denotes the core locations of six mesoscale eddies. The depth range for all images spans from 0 to 1500 m. **c** Location map of seismic lines in **a** (red lines) and **b** (yellow lines).

steps points towards a modest increase with water depth (although not statistically significant; see Supplementary Fig. 2), which bears a resemblance to the diffusive convection staircases in the Arctic Ocean[8]. A previous study using seismic data to image thermohaline staircases east of the Lesser Antilles also found that step thickness increased with depth[35]. Some studies[13,18] have reported that the step thickness of Caribbean Sea staircases shows no distinct dependence on depth, potentially attributed to their limited sample size. The average thickness of these steps is 18.31 ± 2.49 m (Supplementary Fig. 3), aligning remarkably well with the step thickness observed in CTD No.4 and with a previous study on Caribbean Sea staircases[13]. These findings compellingly underscore the effectiveness of utilizing seismic images for the identification and characterization of thermohaline staircases.

The cumulative length of the 26 seismic transects is about 2518 kilometers, with approximately 70% (1751 km) of the horizontal span exhibiting the presence of thermohaline staircases (Supplementary Table 1). This attests to the widespread occurrence of staircases in the region, markedly surpassing the 7% occurrence rate documented in previous investigations of Caribbean Sea staircases[12]. Figure 1 demonstrates the inferred distribution area of staircases based on these seismic images.

Disruption of thermohaline staircases by mesoscale eddies

In addition to the thermohaline staircases, seismic images also show elliptical areas of relatively weaker amplitude reflections (Figs. 3 and 5). These regions, in fact, represent the presence of mesoscale eddies. The kind of lens-shaped reflectors are likely to be anticyclonic eddies[33,37,38].

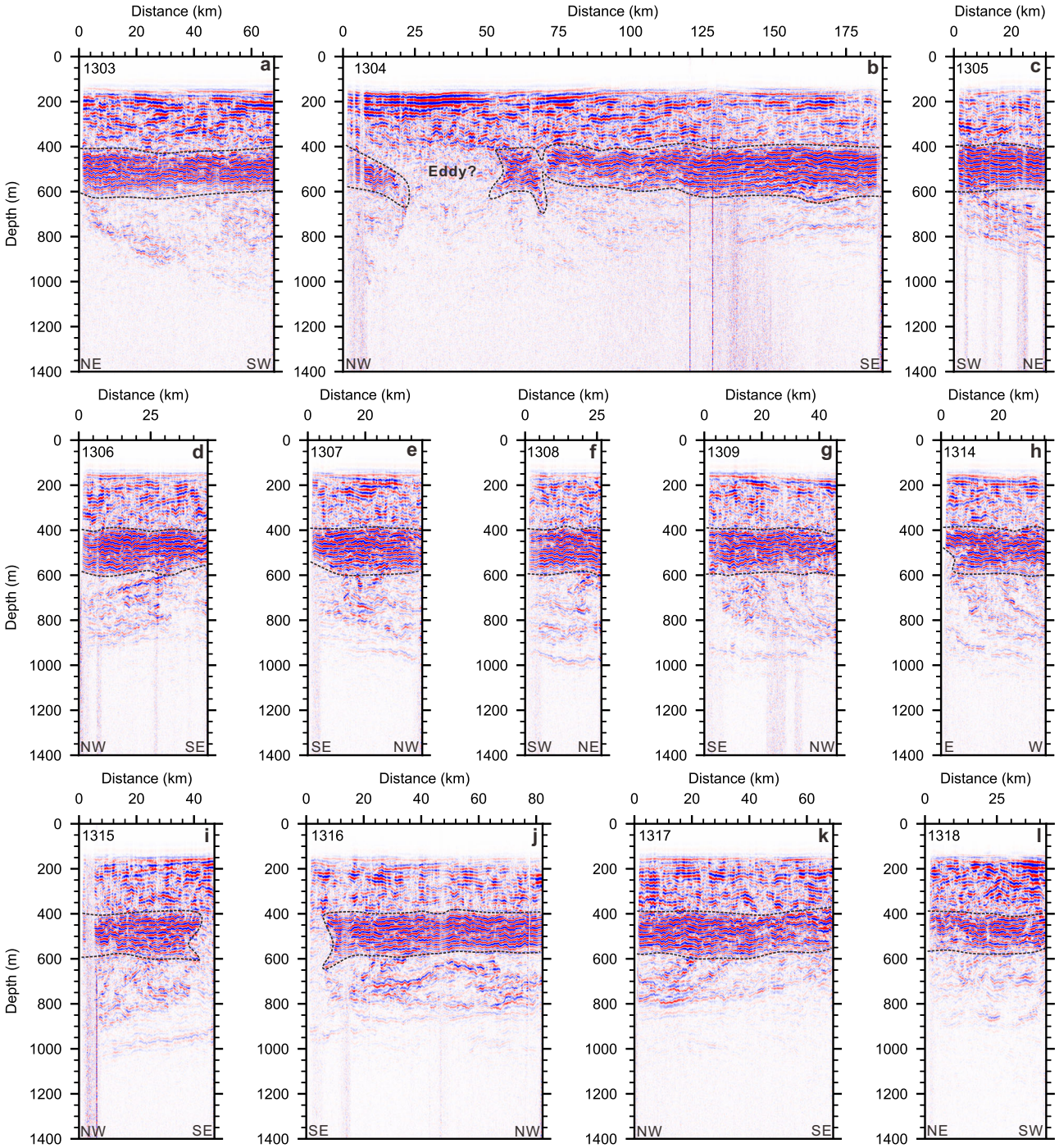

Fig. 4 | Seismic images of coherent thermohaline staircases. These images illustrate a coherent set of thermohaline staircases within the depth range of about 400–600 m. Panels **a**–**l** represent lines 1303–1318, respectively. Black dashed lines outline the boundaries of the staircases.

Based on the theory of geostrophic balance and the thermal wind equation, the vertical shear S of cross-transect horizontal velocity can be estimated by tracking seismic reflectors[39] (see 'Methods'), as shown in Fig. 6. Vertical shear in weak reflection areas, where the seismic signal-to-noise ratio is low, is discarded due to potential errors. The vertical shear of some eddies (e.g., E1) cannot be estimated when the upper boundary does not have effective reflectors. Note that only the geostrophic shear is considered here (and not the cyclogeostrophic shear). The magnitude of cyclogeostrophic shear is larger by only several percent[23]. The geostrophic velocity can be obtained by integrating the geostrophic shear relative to a reference depth. However, because of the discrete distribution of our shear estimation results, no integrals were calculated. Since the velocity shear cannot be estimated within the 0–200 m depth range (there are no effective reflectors), we assume a reference depth for zero geostrophic velocity level at 1200 m deep (the velocity is typically very weak)[37]. The resulting geostrophic velocity values indicate that these eddies are likely anticyclonic, rotating clockwise.

A total of six subsurface mesoscale eddies were captured in these seismic images, and certain eddies (e.g., eddies E4 and E5) were recurrently observed from different locations in multiple seismic images (Figs. 1 and 3). At the periphery of mesoscale eddies, high shear is manifested in seismic images as inclined narrow reflection bands (green lines in Fig. 5). These bands are commonly referred to as filaments or spiral arms[33,40,41]. The shear at the peripheries of eddies can induce turbulent mixing[38].

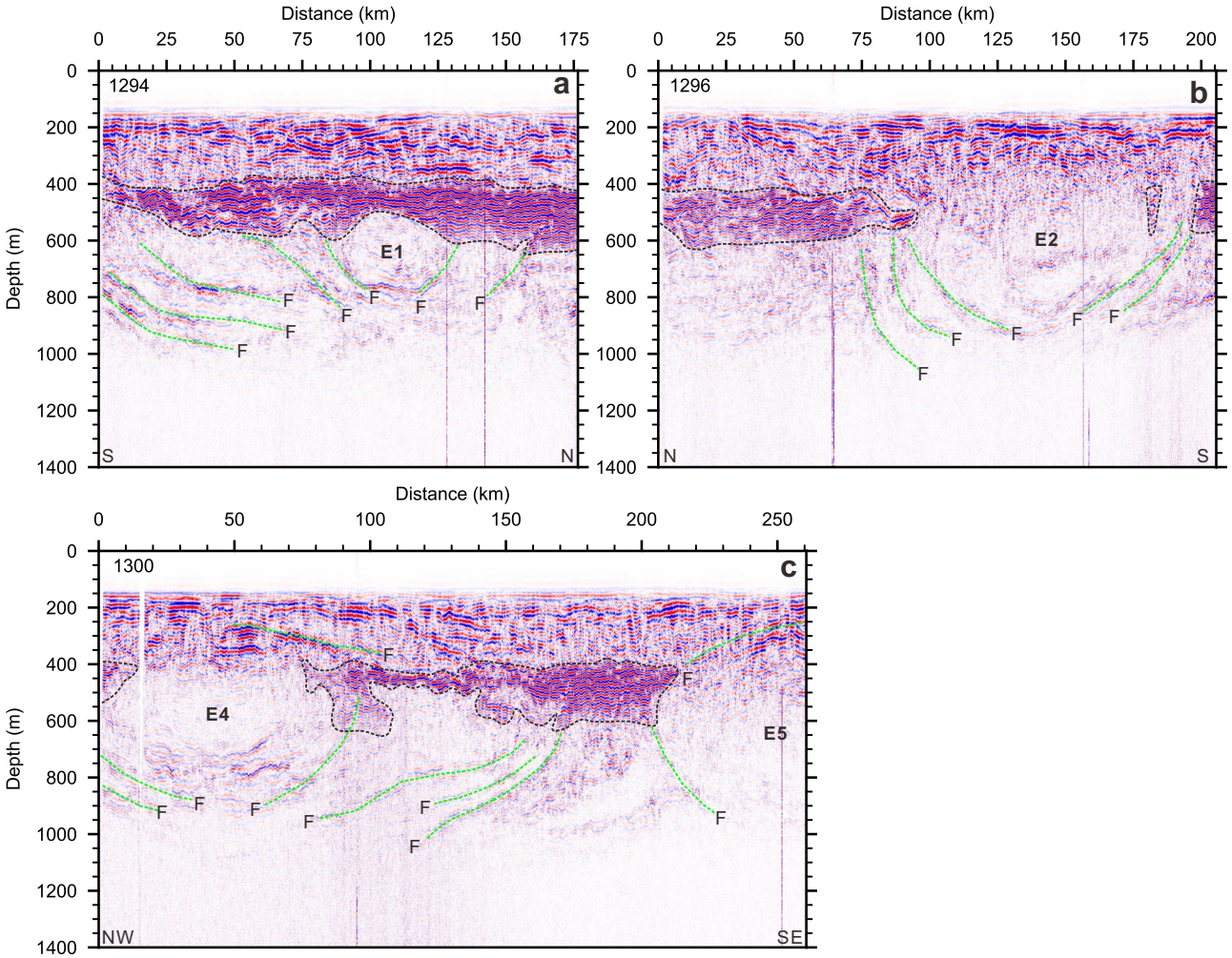

Fig. 5 | Seismic images with thermohaline staircases and mesoscale eddies. Seismic lines **a** 1294, **b** 1296, and **c** 1300 reveal the disruption of thermohaline staircases by mesoscale eddies. Eddy numbers have been marked at the cores of eddies (E1, E2, E4, and E5). Green dashed lines represent the eddy filaments (or spiral arms) at the peripheries of the eddies, labeled as 'F'.

The vertical shears in the staircase regions are relatively weak (close to zero) and notably lower than those at the upper and lower boundaries of the eddies (Fig. 6). We conducted a test using a two-dimensional Gaussian vortex model[42] (see Supplementary Fig. 4), which showed that the vertical shears at the boundaries of the eddies (top-left, top-right, bottom-left, and bottom-right boundaries) are high. The results from the Gaussian vortex model are highly consistent with observations of mesoscale eddies in the Arctic Ocean using concurrent seismic and current velocity data[38]. Although the vertical shear of the Gaussian vortex model is more regular and continuous, it also shares some common features with the estimated shear here, such as exhibiting mainly strong shear at the four corner boundaries of the eddy.

We also estimated the geostrophic Richardson number $\mathrm{Ri} = N^2/S^2$, where N is the buoyancy frequency. Since the buoyancy frequency N is the background value calculated from historical CTD, some errors may arise. The mean relative error of N from 200 to 1000 m is 13.7% (Supplementary Fig. 5), which causes a mean relative error of 29.1% in Ri. When $\mathrm{Ri} < 1/4$, shear instability may occur[43]. Note that smaller regions may have $\mathrm{Ri} < 1/4$, that are not detected, so instability could be occurring even if the estimated Ri here is larger than 1/4. As shown in Fig. 7, regions where $\mathrm{Ri} < 1/4$ are primarily located at the periphery of the eddies, whereas the Ri values in the staircase regions are obviously higher (>1). Although this result is just approximate, it still indicates that the small Ri caused by vertical shear may lead to the disruption of the staircases. Direct numerical simulations of the Arctic Ocean's staircases also show that vertical shear can disrupt the staircases when the Ri of thin layers falls below 1/4[44]. Our observational results corroborate this numerical simulation.

Seismic reflectors can also be used to estimate slope spectra and, subsequently, turbulence diffusivity[45–49] (see 'Methods'). Figure 8 shows the average slope spectra estimated from three seismic transects. The slope spectra in the turbulence subrange exceed the reference slope 1/3, indicating contamination by noise in the turbulence subrange[47]. The spectra of the internal wave subranges for all three transects follow the trend of the GM75 model spectrum[50]. The slope spectrum energy of the internal wave subrange in transect 1294 is significantly lower than that of transects 1296 and 1300, suggesting that the level of internal waves in transect 1294 is lower than in the other two. This can also be visually observed in the seismic transects, where the vertical fluctuations of the staircases in transect 1294 are weaker than those in transects 1296 and 1300, with transect 1300 showing particularly pronounced fluctuations.

Based on the slope spectra of the internal wave subrange, we estimated the vertical diffusivity using fine-scale parameterization (see 'Methods'), representing turbulence mixing induced by internal wave breaking (Fig. 9). Note that the mean relative error of N from 200 to 1000 m, 13.7% (Supplementary Fig. 5), causes a mean relative error of 11.4% in vertical diffusivity. The result indicates that the turbulence diffusivity in the staircase regions is generally lower than in the eddy regions across each transect (Fig. 9b, d, f). The turbulence diffusivity in the staircase regions in transect

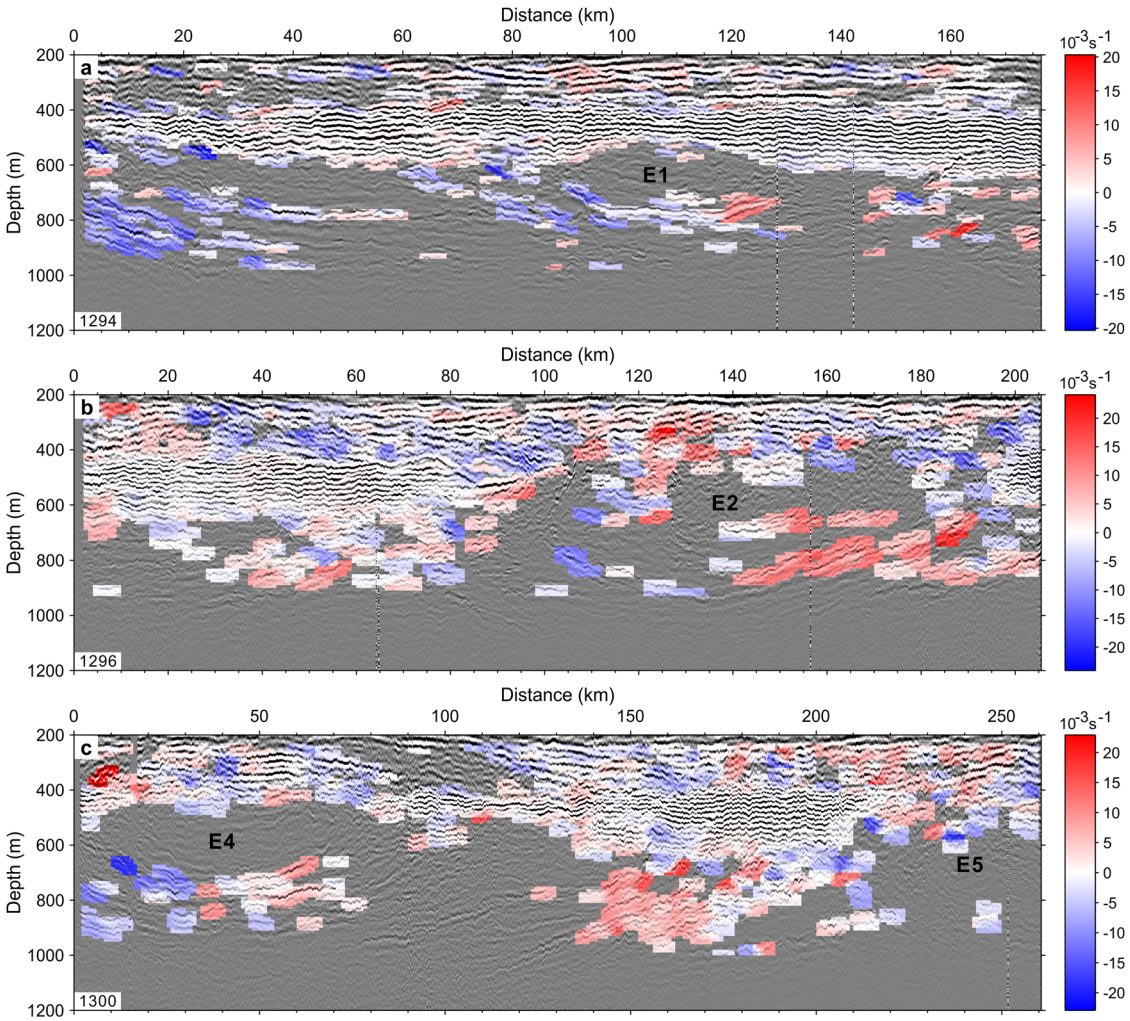

Fig. 6 | Vertical shear of horizontal velocity estimated from seismic data. a–c correspond to seismic lines 1294, 1296, and 1300, respectively. Vertical shears (in color) overlay the seismic transects (in gray). Red and blue indicate outward and inward shears, respectively. Eddy numbers (E1, E2, E4, and E5) have been marked.

1294 is lower than that in transects 1296 and 1300, with transect 1300 showing the highest diffusivity in the staircase regions (Fig. 9b, d, f), which corresponds to the degree of vertical fluctuations of the staircases. The turbulence diffusivity in the staircase regions across all transects is generally below 10^{-5} m^{-2} s^{-1}, whereas at the peripheries of the eddies (except for the upper boundary of eddy E1), it exceeds 10^{-5} m^{-2} s^{-1} (Fig. 9b, d, f). For eddy E1, the weaker turbulence mixing at its edges compared to other eddies may be attributed to a higher Ri (Fig. 7). When turbulence mixing surpasses the double-diffusive mixing driven by salt fingers, staircases are disrupted[10]. The diapycnal diffusivity driven by salt fingers in the Caribbean Sea is about 10^{-5} m^{-2} s^{-1}[51]. These findings strongly suggest that the turbulence mixing induced by vertical shear at the periphery of the eddies disrupts the staircases. Without these subsurface mesoscale eddies, the staircases would maintain lateral coherence (Fig. 4). Although internal waves within the staircases exhibit a certain intensity, the turbulence mixing they cause is insufficient to disrupt the staircases. Staircases are disrupted when the turbulence mixing induced by mesoscale eddy shear exceeds the double-diffusive mixing in the salt finger staircases.

Discussion

The results above considered only the impact of vertical shear from eddies on the disruption of staircases, but horizontal shear (i.e., horizontal stirring) should not be overlooked. Past studies[23,44] appear to have neglected the destructive effects of horizontal shear on staircases. Results from the Gaussian eddy model (see Supplementary Figs. 4 and 6) indicate that the horizontal shear at the periphery of eddies is also relatively high. Although horizontal shear is significantly lower than vertical shear, the horizontal gradients of temperature and salinity are also much smaller than the vertical gradients. Consequently, the disruptive effect of horizontal shear on staircases cannot be ignored. However, estimating horizontal shear from seismic data is challenging and beyond the scope of this paper.

It is also crucial to emphasize that staircases occupy about 70% of the total length of all seismic lines (see Supplementary Table 1), while the remaining 30% is predominantly occupied by the cores of eddies. These results attest to the widespread occurrence of staircases in the region, markedly surpassing the 7% occurrence rate documented in previous investigations of Caribbean Sea staircases[12]. According to previous studies[19,20], energetic anticyclonic eddies in the Caribbean Basin translated westward at ~10 cm s^{-1}. We speculate that, after eddies pass through, areas that initially lacked staircases due to eddy shear gradually readjust their thermohaline distribution, forming new staircases (see Supplementary Fig. 7). Therefore, it is reasonable to infer that in the absence of eddies, staircases may be distributed nearly 100% within the depths of about 400–600 m in this region, as shown in Fig. 1. The inferred area, covered by thermohaline staircases, based on these seismic images is about 3.5×10^4 km^2. This area is substantial even though it is much smaller than the area, about 50×10^4 km^2, covered by staircases in the subtropical Northern Atlantic by the C-SALT survey[52].

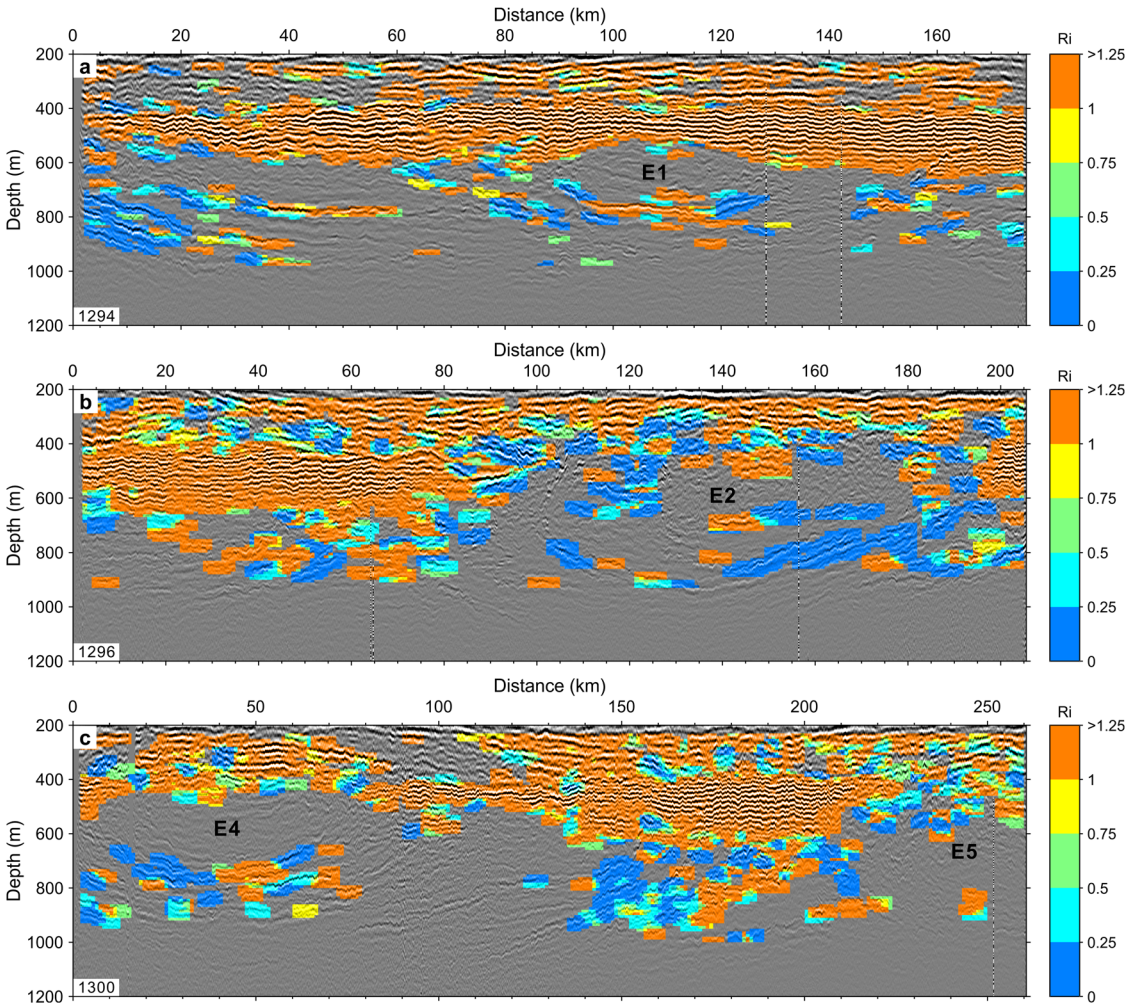

Fig. 7 | Richardson number (Ri) estimated from seismic data. Ri (in color) overlays the seismic transects (in gray). **a**–**c** correspond seismic lines 1294, 1296, and 1300, respectively. The blue areas indicate Ri <0.25, where shear instability is dominant. Eddy numbers (E1, E2, E4, and E5) have been marked.

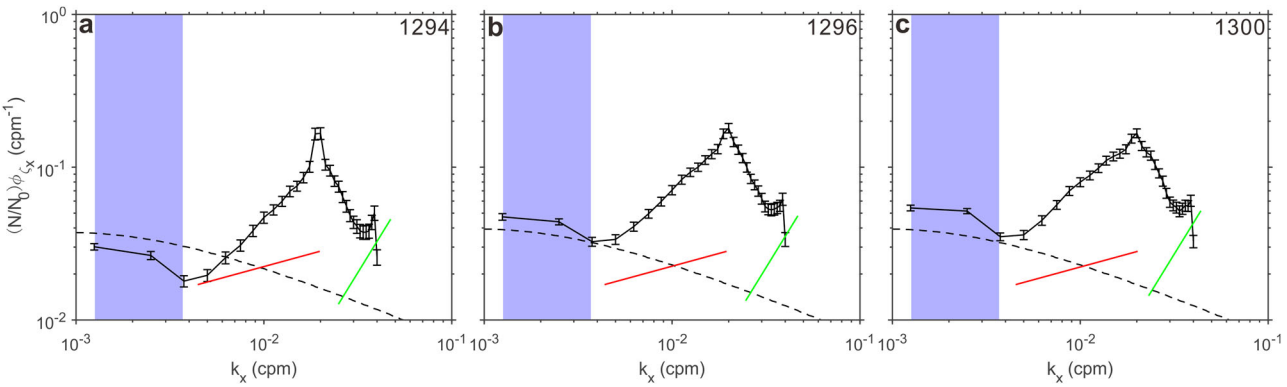

Fig. 8 | Mean slope spectra estimated from seismic reflectors. Panels **a**–**c** correspond to seismic lines 1294, 1296, and 1300, respectively. The slope spectra are normalized by N/N_0. Vertical short lines indicate the 95% confidence interval of the slope spectra. The red and green lines represent reference slopes for turbulence (1/3) and the noise subranges (2), respectively. The black dashed line represents the GM75 towed spectrum. The purple shading denotes the wavenumber range of the internal wave subrange.

In the past, due to limitations in observational sample size and lateral resolution, there has been no consensus on the relationship between eddies and thermohaline staircases. Some studies suggest that thermohaline intrusions at the periphery of eddies can form staircases: lateral gradients create interleaving structures between eddy cores and the background water, eventually evolving into thermohaline staircases[13,22]. However, these observations had a coarse lateral resolution of ~50 km. On the other hand, some studies[24,32] suggest that eddies disrupt staircases, while the limited lateral range of their data undermines the reliability of their conclusions, which also lacks quantitative analysis. When the observational lateral range is insufficient, it is impossible to rule out the possibility that staircases at the periphery of eddies are formed by lateral intrusions between the eddy core

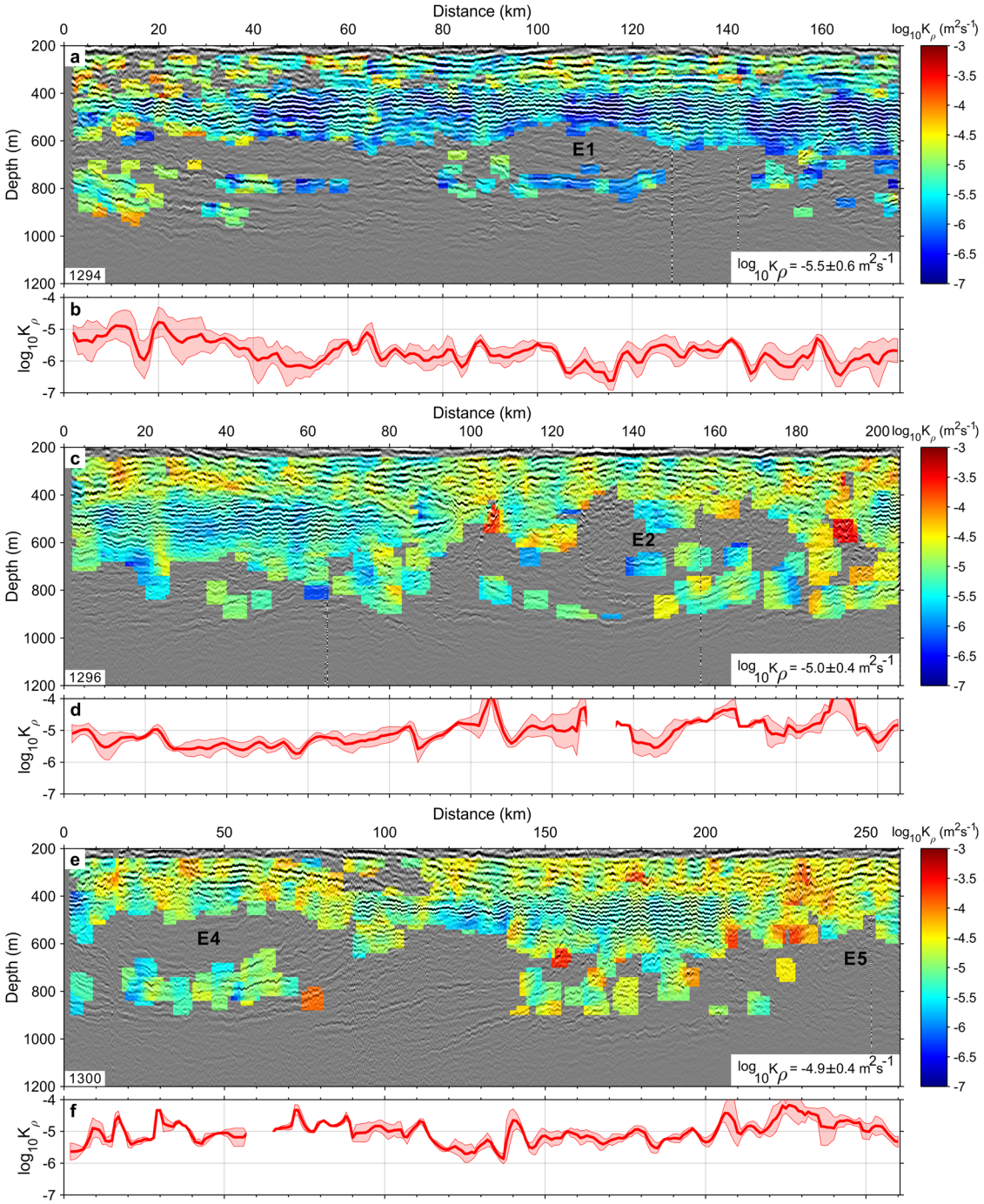

Fig. 9 | Turbulent diffusivity distribution estimated from seismic data. Panels **a**, **c**, **e** show diffusivity (in color) overlaid on seismic transects (in gray) for seismic lines 1294, 1296, and 1300, respectively. The vertical diffusivity is displayed in log10 units. The average and standard deviation of the diffusivity of each transect are marked in the lower right corner. Eddy numbers (E1, E2, E4, and E5) are marked. Panels **b**, **d**, **f** present the mean diffusivity (red line) and standard deviation (red shading) for the depth range of 420–580 m of the three transects.

and the background water. Our study employs multiple seismic transects, with a total length of 2518 km and lateral resolution of ~O (10) m, to nearly simultaneously capture several subsurface mesoscale eddies and thermohaline staircases, revealing their three-dimensional spatial distribution and estimating vertical shear and turbulent diffusivity. The lateral coherence of staircases around these eddies extends over 100 km, making it unlikely that they are formed by lateral intrusions between the eddy core and the background water. These results convincingly demonstrate that the periphery of eddies are not regions where staircases form, but rather areas where they are disrupted.

It is important to emphasize the mixing at eddies' top and bottom boundaries. Previous observations of Mediterranean eddies (Meddies) have shown that diffusive convection and salt-finger convection occur at these top and bottom boundaries, respectively[53–55]. However, temperature and salinity profiles and seismic transects reveal that Meddies' top and bottom boundaries exhibit only a few irregular mixing layers (2–3 layers)[48,54]. In contrast, our study presents multiple, well-defined mixing layers (8–10 layers; Figs. 2, 4, 5), which is a significant distinction from the Meddies' top and bottom boundaries. Our focus is on the staircases at the eddy's lateral peripheries being disrupted by the eddy's vertical shear, not the top and

bottom boundaries. In fact, vertical shear directly above and below the eddy core is indeed weak (indicating weak turbulent mixing; Supplementary Fig. 4), so convective mixing may dominate, which could explain the intact staircases above eddy E1. However, due to the more extensive depth range of other larger eddies (E2–6), staircases are not indicated at the top and bottom boundaries of these larger eddies.

Salt-finger staircases exist within the thermocline of the central basin, where the turbulent mixing is typically weak[14]. These regions exhibit salt-finger-driven double-diffusive mixing, enhancing vertical mixing within the thermocline of the central basin[4]. Subsurface mesoscale eddies with high kinetic energy generate strong shear that induces turbulent mixing, surpassing the double-diffusive mixing driven by salt fingers and consequently disrupting the staircases. The turbulent mixing driven by the eddy shear, being more intense than double-diffusive mixing driven by salt finger (Fig. 9), further enhances the vertical exchange of materials and heat in the region. To the best of our knowledge, previous studies[17,19,20,56–58] have not identified the ubiquity of subsurface mesoscale eddies in the Caribbean Sea, as indicated here. These studies predominantly utilized satellite altimetry and surface drifter data, thereby primarily revealing characteristics of surface eddies while lacking observations and analyses of deeper subsurface eddies. Given this, the properties of the core water of these subsurface mesoscale eddies are also uncertain and require further investigation. The widespread presence of subsurface mesoscale eddies in this area likely plays a crucial role in the transport and redistribution of energy, heat, CO_2, nutrients, and other tracers throughout the Caribbean Sea and possibly the North Atlantic.

Methods

Seismic data acquisition and processing

During the expedition EW9501, conducted by the R/V Maurice Ewing in the eastern Caribbean Sea from February to March 1995, multi-channel seismic data were collected. This study utilizes 26 seismic transects: 1294–1319 (Fig. 1), acquired from February 25 to March 9, 1995 (see Supplementary Table 1). The research vessel towed an 8470 in^3 (~139 L) air gun array, emitting sound waves at about 50 m intervals (i.e., shot spacing). After reflecting at the stratified water column interfaces, the reflected sound waves signals were received by 160 hydrophones along a 3975 m cable. The hydrophone spacing was 25 m, and the minimum distance of the source to the nearest hydrophone (i.e., offset) was 187.5 m. Each hydrophone recorded the reflection signal at a time interval of 2 ms. During the seismic acquisition, the vessel's speed was about 2.5 m s^{-1}. Note that although 160 hydrophones were deployed for receiving acoustic reflection signals during seismic acquisition, the noise was too strong for the hydrophones near the sound source. Therefore, during seismic processing, the nearest 10 hydrophones were discarded, and only 150 hydrophones were used for consequent processing.

Seismic processing followed a standard procedure[59]. The processing workflow employed here aligns closely with a recent study[33] and involves (1) defining the geometry, (2) suppressing direct waves and noise, (3) sound speed analysis, (4) normal move-out correction, (5) stacking, (6) Stolt time migration[60], and (7) noise attenuation. In the seventh step, frequency-domain bandpass filtering and dip filtering in the F–K (frequency–wavenumber) domain were conducted[59]. The frequency-domain bandpass filter utilized a trapezoidal window with a frequency group of 10–20–80–100 Hz. For visualization purposes, the time coordinates of the resulting transects were converted to depth using a conversion speed of 1500 m s^{-1}, which is about the average sound speed for the shallow 1000 m.

Resolutions of seismic data

The horizontal spacing of the hydrophones used to receive the reflected signals is 25 m. Consequently, the lateral sampling interval of the processed seismic data is 12.5 m. This distance is known as the common midpoint (CMP) spacing[59]. However, the lateral sampling interval does not equate to the lateral resolution of seismic data. A previous study[30] briefly outlined the fundamental principles of vertical and horizontal resolution associated with seismic sampling and described the impact of migration on horizontal resolution. The expected horizontal resolution should surpass the first Fresnel zone radius $R_F = \sqrt{\lambda h/2}$, where h is the depth of the reflecting interface, $\lambda = c/f_m$ is the dominant wavelength of the acoustic wave, c is the sound speed, and f_m is the peak frequency of the source wavelet[30,61]. In this study, with a sound speed of about 1500 m s^{-1} and a peak frequency of 35 Hz, the dominant wavelength is 43 m. As the thermohaline staircase exists between 400 and 600 m, the Fresnel radius varies between 93 and 114 m. Migration processing can effectively enhance horizontal resolution[30]. The seismic data's time sampling interval is 2 ms, corresponding to a depth sampling interval of about 1.5 m. Similarly, 1.5 m does not represent the vertical resolution of seismic data. The Rayleigh criterion defines the limit of vertical resolution, indicating the minimum depth interval required to distinguish two sharp reflectors (similar to the ability of an optical system to differentiate between two stars)[61]. According to the Rayleigh criterion, the vertical resolution is approximately 1/4 of the dominant wavelength[61], hence around 11 m. The seismic vertical resolution is less than the step thickness (~18 m) of the Caribbean's staircases, indicating the seismic data's effective resolution of distinct steps.

Historical CTD data

To understand the hydrographic background of the study area, temperature and salinity data from 39 historical CTD (Conductivity, Temperature, Depth) stations were utilized. The data were sourced from the World Ocean Database (https://www.ncei.noaa.gov/access/world-ocean-database-select/dbsearch.html), spanning from August 1997 to April 2021 (Fig. 1). Although the CTD stations are located near the seismic lines, their collection dates vary and do not align with the seismic acquisition date. Nevertheless, we believe these CTD profiles can provide insights into the hydrographic conditions of the region. The vertical sampling interval for temperature and salinity in these CTD profiles is about 2 m, comparable to the seismic data's vertical sampling interval of about 1.5 m.

Calculating Turner angle

The conditions for double-diffusion instability can be characterized by the vertical density ratio $R_\rho = \frac{\alpha T_z}{\beta S_z}$, where α and β are the thermal expansion and salt contraction coefficients respectively, and T_z and S_z represent the vertical gradients of potential temperature and salinity respectively. The Turner angle:

$$\mathrm{Tu} = \tan^{-1}\left(\frac{\alpha T_z - \beta S_z}{\alpha T_z + \beta S_z}\right) \quad (1)$$

is another indicator describing the stability of double-diffusion processes in the water column[62]. Tu functions similarly to density ratio but is more easily visualized graphically, providing a straightforward interpretation of the background tendency for double-diffusion. Tu variations in the water column define the following classification of the stability of the layers: $-90° < \mathrm{Tu} < -45°$ for the diffusive convection regime, $45° < \mathrm{Tu} < 90°$ for the salt-finger regime, $|\mathrm{Tu}| < 45°$ for the stable state, $|\mathrm{Tu}| > 90°$ for the gravitationally unstable state.

Synthetic seismogram

Synthetic seismograms are commonly used in traditional seismic exploration[59,63] and seismic oceanography studies[64,65]. They are generated by convolving the source wavelet with the reflection coefficient, denoted as $x(t) = w(t)^* r(t)$, where $w(t)$, $r(t)$ and $x(t)$ represent the time series of source wavelet, reflection coefficient, and the synthetic seismic trace, respectively, with '*' indicating the convolution operator. In the strata or water columns, the reflection coefficient:

$$r_i = \frac{\rho_{i+1}c_{i+1} - \rho_i c_i}{\rho_{i+1}c_{i+1} + \rho_i c_i} \quad (2)$$

for the ith interface, where c_{i+1} and c_i (or ρ_{i+1} and ρ_i) are the sound speeds (or densities) below and above the interface, respectively[25]. For simplicity, a zero-phase Ricker wavelet $w(t) = [1 - 2(f_m t\pi)^2]e^{-(f_m t\pi)^2}$ is commonly used in the convolution operation, with f_m as the dominant frequency[66]. In this study, the dominant frequency of the seismic data is about 35 Hz. As seawater sound speed and density are functions of temperature and salinity, synthetic seismograms establish a connection between temperature/salinity data and seismic images (Fig. 2 and Supplementary Fig. 8). For salt-fingering staircases, the reflection coefficients at the interface are negative, corresponding to negative values (in blue) on the synthetic seismogram; due to wavelet effects, the uniform mixed layer roughly corresponds to positive polarity (in red) on the synthetic seismogram (Fig. 2 and Supplementary Fig. 8).

Estimating geostrophic shear

In the case of geostrophic balance, the Coriolis force balances the horizontal pressure gradient. Based on the standard thermal wind equation, the vertical shear S of the horizontal velocity perpendicular to the two-dimensional transect is determined by the slope of isopycnals[39], given by:

$$S = \frac{g}{f\rho}\frac{\partial \rho}{\partial z}\tan\gamma \tag{3}$$

where $g = 9.8\ \mathrm{m\ s^{-2}}$ is the gravitational acceleration, $f = 4 \times 10^{-5}\ \mathrm{s^{-1}}$ is the local Coriolis parameter, ρ is density, and γ is the slope of the isopycnal surface. Here, density ρ is calculated using historical CTD data. Within 4 h, seismic reflectors can be approximated as isopycnals[39,67]. In our work, the vessel speed is ~2.5 m s^{-1}, hence reflectors shorter than 36 km track isopycnal surfaces. Then, the slope of the isopycnal can be estimated using seismic reflectors, and hence, the geostrophic shear S can be obtained. The specific calculation workflow follows previous methods[37,39]. In regions with weak-amplitude reflectors, the seismic data have low signal-to-noise ratios, leading to high uncertainties; hence, shear in regions with reflection amplitudes below a given threshold is discarded.

Average slope spectrum

Seismic reflectors over a certain length range can be approximated as isopycnals[68]. By tracking the depth variations of reflectors longer than 1600 m and subtracting the linear trend, the vertical displacements of isopycnals ζ are obtained[39,69]. Using a 64-point (800 m) Hanning window, a Fourier transform is then performed to compute the horizontal wavenumber spectrum $\phi_\zeta(k_x)$ via the Welch method[69]. To differentiate between internal wave and turbulence regimes, the spectrum of horizontal gradients of vertical displacement, i.e., slope spectrum $\phi_{\zeta_x} = (2\pi k_x)^2\phi_\zeta$, is analyzed. The slope spectrum in the internal wave regime has a negative slope, while in the turbulence regime, the slope is positive with a reference slope of 1/3. To eliminate the dependency of internal wave displacement on local stratification[39], the slope spectrum is multiplied by N/N_0, where N is the average buoyancy frequency, derived from historical CTD data, within the depth range of the selected reflector, and $N_0 = 5.2 \times 10^{-3}\ \mathrm{s^{-1}}$.

Estimating vertical turbulent diffusivity

Using fine-scale parameterization, we can estimate the turbulence dissipation rate[45–49]. The slope of the spectrum in the turbulent subrange exceeds the reference slope 1/3, indicating noise contamination. Therefore, we use the slope spectrum in the internal wave subrange to estimate the dissipation rate, representing the turbulence mixing caused by internal wave breaking[47,48]. We employ the following equation:

$$\varepsilon = \varepsilon_0 \frac{N^2}{N_0^2 f_0}\frac{f\ \cosh(N/f)}{\cosh(N_0/f_0)}\frac{R_\omega(R_\omega+1)}{12}\sqrt{\frac{2}{R_\omega - 1}}\left\langle \frac{\phi_{\zeta_x}^{IW}}{\phi_{\zeta_x}^{GM}}\right\rangle^2 \tag{4}$$

where $\varepsilon_0 = 7 \times 10^{-10}\ \mathrm{W\ kg^{-1}}$ is the reference dissipation rate, N is the average buoyancy frequency (from historical CTD data) at the depth of the selected reflector, $N_0 = 5.2 \times 10^{-3}\ \mathrm{s^{-1}}$, f and f_0 are the Coriolis frequencies at the current latitude and 30° latitude, respectively, R_ω is the shear-to-strain ratio, $\phi_{\zeta_x}^{IW}$ and $\phi_{\zeta_x}^{GM}$ are slope spectrum and Garrett–Munk model spectrum[50] of the internal wave subrange, respectively, and <·> denotes averaging operator. Due to the lack of in-situ R_ω values, we use the global average $R_\omega = 7$[46]. Finally, we obtain the vertical diffusivity using the Osborn method[70]:

$$K_\rho = \Gamma\varepsilon/N^2 \tag{5}$$

where Γ is the mixing efficiency. For turbulent mixing, we use an average value of Γ = 0.2. Note that this estimation pertains to turbulence mixing caused by internal wave breaking and does not include salt-finger-induced diffusive mixing.

Data availability

The raw multi-channel seismic reflection data are provided by the Marine Geoscience Data System and available at https://www.marine-geo.org/tools/search/Files.php?data_set_uid=3752. Seismic images of the processed seismic data are available at https://github.com/shunyangchina/ew9501/tree/seismic_images. The estimated vertical shear, Richardson number, and vertical diffusivity data are available at https://github.com/shunyangchina/ew9501/tree/estimated_data. Thirty-nine historical CTD data are downloaded from the World Ocean Database (https://www.ncei.noaa.gov/access/world-ocean-database-select/dbsearch.html), and available at https://github.com/shunyangchina/ew9501/tree/CTD.

Code availability

The MATLAB code for the estimations of vertical shear, Richardson number and vertical diffusivity is available on request to the corresponding author. The maps in Figs. 1, 3c are created with M_map (version 14.0; https://www.eoas.ubc.ca/~rich/map.html) and MATLAB (version 2019a). All images are created with MATLAB (version 2019a) and Python (version 3.10.9).

Received: 10 April 2024; Accepted: 23 July 2024;
Published online: 30 July 2024

References

1. Kelley, D. E., Fernando, H. J. S., Gargett, A. E., Tanny, J. & Ozsoy, E. The diffusive regime of double-diffusive convection. *Prog. Oceanogr.* **56**, 461–481 (2003).
2. Schmitt, R. W. Double diffusion in oceanography. *Annu. Rev. Fluid Mech.* **26**, 255–285 (1994).
3. Stern, M. E. The "Salt-Fountain" and thermohaline convection. *Tellus* **12**, 172–175 (1960).
4. Schmitt, R. W., Ledwell, J. R., Montgomery, E. T., Polzin, K. L. & Toole, J. M. Enhanced diapycnal mixing by salt fingers in the thermocline of the tropical Atlantic. *Science* **308**, 685–688 (2005).
5. Timmermans, M. L., Toole, J., Krishfield, R. & Winsor, P. Ice-Tethered Profiler observations of the double-diffusive staircase in the Canada Basin thermocline. *J. Geophys. Res. Oceans* **113**, C00A02 (2008).
6. Shibley, N. C., Timmermans, M. L., Carpenter, J. R. & Toole, J. M. Spatial variability of the Arctic Ocean's double-diffusive staircase. *J. Geophys. Res. Oceans* **122**, 980–994 (2017).
7. Stranne, C. et al. Acoustic mapping of thermohaline staircases in the Arctic Ocean. *Sci. Rep.* **7**, 1–9 (2017).
8. Lu, Y. Z., Guo, S. X., Zhou, S. Q., Song, X. L. & Huang, P. Q. Identification of thermohaline sheet and its spatial structure in the Canada Basin. *J. Phys. Oceanogr.* **52**, 2773–2787 (2022).
9. Tait, R. I. & Howe, M. R. Thermohaline staircase. *Nature* **231**, 178–179 (1971).
10. St Laurent, L. & Schmitt, R. W. The contribution of salt fingers to vertical mixing in the North Atlantic Tracer Release Experiment. *J. Phys. Oceanogr.* **29**, 1404–1424 (1999).

11. Rollo, C., Heywood, K. J. & Hall, R. A. Glider observations of thermohaline staircases in the tropical North Atlantic using an automated classifier. *Geosci. Instrum. Methods* **11**, 359–373 (2022).
12. van der Boog, C. G., Dijkstra, H. A., Pietrzak, J. D. & Katsman, C. A. Spatial variations of Antarctic Intermediate Water in the Caribbean Sea due to vertical mixing along its path. *Geophys. Res. Lett.* **49**, 2021GL095977 (2022).
13. Morell, J. M., Corredor, J. E. & Merryfield, W. J. Thermohaline staircases in a Caribbean eddy and mechanisms for staircase formation. *Deep Sea Res. Part II* **53**, 128–139 (2006).
14. Durante, S. et al. Permanent thermohaline staircases in the Tyrrhenian Sea. *Geophys. Res. Lett.* **46**, 1562–1570 (2019).
15. Buffett, G. G. et al. Seismic oceanography in the Tyrrhenian Sea: thermohaline staircases, eddies, and internal waves. *J. Geophys. Res.* **122**, 8503–8523 (2017).
16. Lambert, R. B. & Sturges, W. A thermohaline staircase and vertical mixing in the thermocline. *Deep Sea Res.* **24**, 211–222 (1977).
17. van der Boog, C. G. et al. Hydrographic and biological survey of a surface-intensified anticyclonic eddy in the Caribbean Sea. *J. Geophys. Res.* **124**, 6235–6251 (2019).
18. Corredor, J. E., Morell, J. M., López, J. M., Capella, J. E. & Armstrong, R. A. Cyclonic eddy entrains Orinoco River Plume in eastern Caribbean. *Eos Trans. Am. Geophys. Union* **85**, 197–202 (2004).
19. Richardson, P. L. Caribbean current and eddies as observed by surface drifters. *Deep Sea Res. Pt II* **52**, 429–463 (2005).
20. Lopez-Alzate, M. E. et al. Mesoscale eddy variability in the Caribbean Sea. *Ocean Dyn.* **72**, 679–693 (2022).
21. Andrade, C. A. & Barton, E. D. The Guajira upwelling system. *Cont. Shelf Res.* **25**, 1003–1022 (2005).
22. Merryfield, W. J. Origin of thermohaline staircases. *J. Phys. Oceanogr.* **30**, 1046–1068 (2000).
23. Bebieva, Y. & Timmermans, M. L. An examination of double-diffusive processes in a mesoscale eddy in the Arctic Ocean. *J. Geophys. Res.* **121**, 457–475 (2016).
24. Biescas, B., Armi, L., Sallares, V. & Gracia, E. Seismic imaging of staircase layers below the Mediterranean Undercurrent. *Deep Sea Res. Part I* **57**, 1345–1353 (2010).
25. Shibley, N. C., Timmermans, M. L. & Stranne, C. Analysis of acoustic observations of double-diffusive finestructure in the Arctic Ocean. *Geophys. Res. Lett.* **47**, e2020GL089845 (2020).
26. Song, H. et al. Progress and prospects of seismic oceanography. *Deep Sea Res. Part I* **177**, 103631 (2021).
27. Dickinson, A. & Gunn, K. L. The next decade of seismic oceanography: possibilities, challenges and solutions. *Front. Mar. Sci.* **9**, 736693 (2022).
28. Holbrook, W. S., Paramo, P., Pearse, S. & Schmitt, R. W. Thermohaline fine structure in an oceanographic front from seismic reflection profiling. *Science* **301**, 821–824 (2003).
29. Sheen, K. L., White, N. J., Caulfield, C. P. & Hobbs, R. W. Seismic imaging of a large horizontal vortex at abyssal depths beneath the Sub-Antarctic Front. *Nat. Geosci.* **5**, 542–546 (2012).
30. Ruddick, B., Song, H. B., Dong, C. Z. & Pinheiro, L. Water column seismic images as maps of temperature gradient. *Oceanography* **22**, 192–205 (2009).
31. Sallares, V. et al. Relative contribution of temperature and salinity to ocean acoustic reflectivity. *Geophys. Res. Lett.* **36**, L00D06 (2009).
32. Biescas, B. et al. Imaging meddy finestructure using multichannel seismic reflection data. *Geophys. Res. Lett.* **35**, L11609 (2008).
33. Yang, S., Song, H., Coakley, B., Zhang, K. & Fan, W. A mesoscale eddy with submesoscale spiral bands observed from seismic reflection sections in the Northwind Basin, Arctic Ocean. *J. Geophys. Res.* **127**, e2021JC017984 (2022).
34. Yang, S., Song, H. B., Fan, W. H. & Wu, D. Submesoscale features of a cyclonic eddy in the Gulf of Papagayo, Central America. *Chin. J. Geophys.* **64**, 1328–1340 (2021).
35. Fer, I., Nandi, P., Holbrook, W. S., Schmitt, R. W. & Paramo, P. Seismic imaging of a thermohaline staircase in the western tropical North Atlantic. *Ocean Sci.* **6**, 621–631 (2010).
36. Meng, L. et al. Discovery of thermohaline staircases in the Gulf of California. *Chin. J. Geophys.* **66**, 1634–1648 (2023).
37. Tang, Q. S., Gulick, S. P. S., Sun, J., Sun, L. & Jing, Z. Submesoscale features and turbulent mixing of an oblique anticyclonic eddy in the Gulf of Alaska investigated by marine seismic survey data. *J. Geophys. Res.* **125**, e2019JC015393 (2020).
38. Yang, S., Song, H., Coakley, B. & Zhang, K. Enhanced mixing at the edges of mesoscale eddies observed from high-resolution seismic data in the western Arctic Ocean. *J. Geophys. Res.* **128**, e2023JC019964 (2023).
39. Sheen, K. L., White, N., Caulfield, C. P. & Hobbs, R. W. Estimating geostrophic shear from seismic images of oceanic structure. *J. Atmos. Ocean Tech.* **28**, 1149–1154 (2011).
40. Song, H., Pinheiro, L. M., Ruddick, B. & Teixeira, F. C. Meddy, spiral arms, and mixing mechanisms viewed by seismic imaging in the Tagus Abyssal Plain (SW Iberia). *J. Mar. Res* **69**, 827–842 (2011).
41. Ménesguen, C. et al. Arms winding around a meddy seen in seismic reflection data close to the Morocco coastline. *Geophys. Res. Lett.* **39**, L05604 (2012).
42. von Appen, W. J., Pickart, R. S., Brink, K. H. & Haine, T. W. N. Water column structure and statistics of Denmark Strait Overflow Water cyclones. *Deep Sea Res. Pt I* **84**, 110–126 (2014).
43. Thorpe S. A. *An Introduction to Ocean Turbulence*. (Cambridge University Press, 2007).
44. Brown, J. M. & Radko, T. Disruption of Arctic staircases by shear. *Geophys. Res. Lett.* **49**, e2022GL100605 (2022).
45. Gregg, M. C., Sanford, T. B. & Winkel, D. P. Reduced mixing from the breaking of internal waves in equatorial waters. *Nature* **422**, 513–515 (2003).
46. Kunze, E., Firing, E., Hummon, J. M., Chereskin, T. K. & Thurnherr, A. M. Global abyssal mixing inferred from lowered ADCP shear and CTD strain profiles. *J. Phys. Oceanogr.* **36**, 1553–1576 (2006).
47. Dickinson, A., White, N. J. & Caulfield, C. P. Spatial variation of diapycnal diffusivity estimated from seismic imaging of internal wave field, Gulf of Mexico. *J. Geophys. Res.* **122**, 9827–9854 (2017).
48. Xiao, W. & Meng, Z. Turbulent heat fluxes in a Mediterranean eddy quantified using seismic and hydrographic observations. *J. Mar. Sci. Eng.* **10**, 720 (2022).
49. Sheen, K. L., White, N. J. & Hobbs, R. W. Estimating mixing rates from seismic images of oceanic structure. *Geophys. Res. Lett.* **36**, L00D04 (2009).
50. Garrett, C. & Munk, W. Space-time scales of internal waves: a progress report. *J. Geophys. Res.* **80**, 291–297 (1975).
51. van der Boog, C. G., Dijkstra, H. A., Pietrzak, J. D. & Katsman, C. A. Double-diffusive mixing makes a small contribution to the global ocean circulation. *Commun. Earth Environ.* **2**, 46 (2021).
52. Schmitt, R. W., Perkins, H., Boyd, J. D. & Stalcup, M. C. C-SALT: an investigation of the thermohaline staircase in the western tropical North Atlantic. *Deep Sea Res.* **34**, 1655–1665 (1987).
53. Ruddick, B. Intrusive mixing in a Mediterranean salt lens—intrusion slopes and dynamic mechanisms. *J. Phys. Oceanogr.* **22**, 1274–1285 (1992).
54. Hebert, D. Estimates of salt-finger fluxes. *Deep-Sea Res. Part A* **35**, 1887–1901 (1988).
55. Hebert, D., Oakey, N. & Ruddick, B. Evolution of a Mediterranean salt lens: scalar properties. *J. Phys. Oceanogr.* **20**, 1468–1483 (1990).
56. Andrade, C. A. & Barton, E. D. Eddy development and motion in the Caribbean Sea. *J. Geophys. Res.* **105**, 26191–26201 (2000).
57. Rudzin, J. E., Shay, L. K., Jaimes, B. & Brewster, J. K. Upper ocean observations in eastern Caribbean Sea reveal barrier layer within a warm core eddy. *J. Geophys. Res.* **122**, 1057–1071 (2017).

58. van der Boog, C. G. et al. The impact of upwelling on the intensification of anticyclonic ocean eddies in the Caribbean Sea. *Ocean Sci.* **15**, 1419–1437 (2019).
59. Yilmaz O. *Seismic Data Analysis: Processing, Inversion, and Interpretation of Seismic Data*. (Society of Exploration Geophysicists, 2001).
60. Stolt, R. H. Migration by Fourier-transform. *Geophysics* **43**, 23–48 (1978).
61. Sheriff R. E., Geldart L. P. *Exploration Seismology*, 2nd edn. (Cambridge University Press, 1995).
62. Ruddick, B. A practical indicator of the stability of the water column to double-diffusive activity. *Deep Sea Res.* **30**, 1105–1107 (1983).
63. Kelly, K. R., Ward, R. W., Treitel, S. & Alford, R. M. Synthetic seismograms: a finite-difference approach. *Geophysics* **41**, 2–27 (1976).
64. Sarkar, S. et al. Seismic reflection imaging of mixing processes in Fram Strait. *J. Geophys Res.* **120**, 6884–6896 (2015).
65. Cooper, J. K., Gorman, A. R., Bowman, M. H. & Smith, R. O. Temporal variability of thermohaline fine-structure associated with the Subtropical Front off the Southeast Coast of New Zealand in high-frequency short-streamer multi-channel seismic data. *Front. Mar. Sci.* **8**, 751385 (2021).
66. Ricker, N. Wavelet contraction, wavelet expansion, and the control of seismic resolution. *Geophysics* **18**, 769–792 (1953).
67. Krahmann, G., Papenberg, C., Brandt, P. & Vogt, M. Evaluation of seismic reflector slopes with a Yoyo-CTD. *Geophys. Res Lett.* **36**, L00D02 (2009).
68. Krahmann, G., Brandt, P., Klaeschen, D. & Reston, T. Mid-depth internal wave energy off the Iberian Peninsula estimated from seismic reflection data. *J. Geophys. Res.* **113**, C12016 (2008).
69. Holbrook, W. S. et al. Estimating oceanic turbulence dissipation from seismic images. *J. Atmos. Ocean Tech.* **30**, 1767–1788 (2013).
70. Osborn. Estimates of the local rate of vertical diffusion from dissipation measurements. *J. Phys. Oceanogr.* **10**, 83–89 (1980).

Acknowledgements

The authors are very grateful to all scientists and crew members of R/V Maurice Ewing expedition EW9501 for their contributions to the acquisition of multi-channel seismic data. The seismic data acquisition was funded by the US National Science Foundation (Grant OCE93-02578). This work was funded by the National Natural Science Foundation of China (Grants 42176061, 41976048, and 42306063). The authors also thank Dr. Katy Sheen and an anonymous reviewer for their valuable comments on this article.

Author contributions

S.Y. and K.Z. wrote the initial paper, performed the data processing and analysis, and revised the paper. H.S. planned the research, provided guidance for the data analysis, and revised the paper. B.R. contributed to paper revision. M.L. and L.M. contributed to the data analysis. S.Y. and K.Z. contribute equally to this article.

Competing interests

The authors declare no competing interests.

Additional information

Supplementary information The online version contains supplementary material available at https://doi.org/10.1038/s43247-024-01577-3.

Correspondence and requests for materials should be addressed to Haibin Song.

Peer review information *Communications Earth & Environment* thanks Katy Sheen and the other, anonymous, reviewer(s) for their contribution to the peer review of this work. Primary Handling Editor: Alireza Bahadori. A peer review file is available.

Reprints and permissions information is available at http://www.nature.com/reprints

Publisher's note Springer Nature remains neutral with regard to jurisdictional claims in published maps and institutional affiliations.

Open Access This article is licensed under a Creative Commons Attribution-NonCommercial-NoDerivatives 4.0 International License, which permits any non-commercial use, sharing, distribution and reproduction in any medium or format, as long as you give appropriate credit to the original author(s) and the source, provide a link to the Creative Commons licence, and indicate if you modified the licensed material. You do not have permission under this licence to share adapted material derived from this article or parts of it. The images or other third party material in this article are included in the article's Creative Commons licence, unless indicated otherwise in a credit line to the material. If material is not included in the article's Creative Commons licence and your intended use is not permitted by statutory regulation or exceeds the permitted use, you will need to obtain permission directly from the copyright holder. To view a copy of this licence, visit http://creativecommons.org/licenses/by-nc-nd/4.0/.

© The Author(s) 2024